ADVANCED FUNCTIONAL MATERIALS
www.afm-journal.de

Materials Views
www.MaterialsViews.com

Pulsed Laser Ablation Based Synthesis of PbS-Quantum Dot-Decorated One-Dimensional Nanostructures and Their Direct Integration into Highly Efficient Nanohybrid Heterojunction-Based Solar Cells

I. Ka, B. Gonfa, V. Le Borgne, D. Ma, and M. A. El Khakani**

The pulsed laser deposition (PLD) technique is used for the direct fabrication of nanohybrid heterojunctions (NH-HJs) solar cells exhibiting high PCE and excellent stability in air without any encapsulation and/or resorting to any surface treatment, ligand engineering and/or post-synthesis processing. The NH-HJs are achieved through the PLD-based decoration of hydrothermally-grown one-dimensional TiO_2 nanorods (TiO_2-NRs) by PbS quantum dots (PbS-QDs). By optimizing both the amount of PbS-QDs (via the number of laser ablation pulses) and the length of the TiO_2-NRs, it is possible to achieve optimal NH-HJs based PV devices with high power conversion efficiency (PCE) of 4.85%. This high PCE is found to occur for an optimal length of the NRs (≈290 nm) which coincides with the average penetration depth of PbS-QDs into the porous TiO_2-NRs matrix, leading thereby to the formation of the largest extent of NH-HJs. Most importantly, the PCE of these novel devices is found to be fairly stable for several months under ambient air. The addition of single-wall carbon nanotubes (SWCNTs) onto the TiO_2-NRs prior to their decoration by PbS-QDs is shown to further enhance their PCE to a value as high as 5.3%, because of additional light absorption and improved charge collection ensured by SWCNTs.

1. Introduction

The growing needs for sustainable energy sources have made very attractive the research on solar cells involving semiconductor quantum dots (QDs). Over the two past decades, lead chalcogenide (PbS, PbSe, etc.) QDs have attracted a great deal of interest[1–7] particularly because of their ability to exploit the NIR region of the sunlight spectrum.[5,7] This advantageous feature is mainly due to the possibility of tuning the band gap of these QDs through the control of their size.[2,6] Moreover, the recent observation of multiple exciton-generation in chalcogenide QDs[6,8] has added impetus to their very promising use for novel highly-efficient photovoltaic (PV) devices. On the other hand, two major recent advances have been made in colloidal quantum dot solar cells, namely: 1) the long insulating ligands surrounding the QDs, required for solution processability, have been replaced by very short monovalent halide anions;[9] and 2) the compact and continuous TiO_2 films, commonly used as electrodes, were replaced by TiO_2 nanowires (NWs).[10] Thus, by infiltrating the chemically prepared QDs solutions through TiO_2 nanowire arrays, charge transfer can be ensured between QDs and TiO_2 NWs, which in turn has led to the development of solar cells with relatively high power conversion efficiencies (PCE).[9,10] Despite these promising PCE achievements, solution processing of QDs remains rather complicated and the resulting QDs generally exhibit poor stability in air, making thereby mandatory the encapsulation of the solar cells in a controlled environment or in a glove box for a long-term use.[4,9,10] This translates into additional fabrication costs and complicates the devices storage and their long-term utilization. Therefore, there is a need to develop new fabrication strategies of QDs that will circumvent such limitations by enabling the in-situ growth of QDs onto various nanostructures and thus their facile integration into high-performance and stable PV devices. In a previous paper, we have demonstrated the powerfulness and process latitude of the pulsed laser deposition (PLD) technique to decorate controllably single-wall carbon nanotubes (SWCNTs) with PbS-QDs in order to achieve PbS-QDs/SWCNTs nanohybrids (NHs) with unparalleled photoconductive properties.[11] Indeed, the in-situ growth of PbS-QDs directly onto the surface of the nanotubes, by means of the energetic PLD process, ensures direct atomic contacts between QDs and SWCNTs, which have resulted in very efficient and fast charge transfer from the light absorbing QDs to the charge conveying nanotubes.[11] Pulsed laser deposition definitely offers a highly attractive alternative for the controlled synthesis of highly-crystalline nanoparticles onto various substrates and nano-architectures.[11–16] Indeed, it can be used advantageously to achieve local and controllable decoration of virtually any kind of nanostructures by desired nanoparticles, without the need of

I. Ka, B. Gonfa, Dr. V. Le Borgne, Prof. D. Ma, Prof. M. A. El Khakani
Institut National de la Recherche Scientifique
INRS-Énergie, Matériaux et Télécommunications
1650, Blvd. Lionel–Boulet
C.P. 1020 J3X-1S2, Varennes, Qc, Canada
E-mail: elkhakani@emt.inrs.ca

DOI: 10.1002/adfm.201304191

using any multi-step chemical post processing, and/or dealing with ligands engineering with their limited charge transfer and poor-stability drawbacks.

In this paper, by capitalizing on the advantageous features of the PLD approach together with other device architecture strategies (including optimization of TiO_2 nanorod characteristics, introduction of hole extracting layer (HEL), and improvement of charge transfer through SWCNTs incorporation), we were able to achieve, for the first time, nanohybrids heterojunctions (NH-HJs) solar cells exhibiting high PCE and excellent stability in air without any encapsulation. The NH-HJs consist of PbS-QDs PLD-grown directly onto hydrothermally prepared one-dimensional (1D) TiO_2-nanorods (uncoated and spray-coated with SWCNTs). The optimized growth of the TiO_2-nanorods (NRs) onto FTO substrates together with their subsequent conformal decoration by PLD-deposited PbS-QDs has led to the formation of novel NH-HJs, which were straightforwardly integrated into PV devices. We were thus able to demonstrate the potential of this PLD-based approach by achieving ambient-air stable NH-HJs solar cells exhibiting a high PCE of 4.85%. In addition, spray-coating of SWCNTs onto the TiO_2-NRs prior to their decoration by PbS-QDs was found to further increase the PCE of the NH-HJs PV devices to a value as high as 5.3% because of additional light absorption and improved charge collection provided by the SWCNTs.

2. Results and Discussion

The TiO_2-NRs films were grown onto transparent conductive fluorine-doped tin oxide covered glass (FTO-glass) substrates precoated with a sputter-deposited thin TiO_2 seed layer (≈40 nm-thick). The deposition conditions of the TiO_2 seed layer together with the details of the hydrothermal synthesis of the TiO_2-NRs are described in the Experimental Section. **Figure 1**a shows a typical top-view scanning electron microscopy (SEM) image of the TiO_2-NRs. The TiO_2-NRs are seen to grow uniformly all over the substrate surface with an evident porosity between them. The cross-sectional SEM view (inset of Figure 1a) shows that the TiO_2-NRs are vertically aligned with a very slight tilt. The NRs are square-shaped (with a side dimension varying from 70 to 140 nm and inter-distance ranging from 250 to 100 nm as the growth time is increased). The growth time was used to control the length of TiO_2-NRs, which was varied in the (100–2500) nm range. The TiO_2 seed layer was found to enhance significantly the adhesion of the NRs to the FTO substrates, and efficiently prevent their occasional peeling-off observed without its use, in accordance with previous reports.[17,18] The X-ray diffraction (XRD) analysis of the TiO_2-NRs (Figure 1b) confirmed their crystalline nature, as they were found to exhibit the characteristic peaks of the rutile phase. The relatively sharp XRD peaks of Figure 1b suggest a high cristallinity of the TiO_2-NRs. Indeed, high-resolution transmission electron microscopy (HR-TEM) observations of single TiO_2-NR revealed their monocrystalline nature, as illustrated in Figure 1c where the lattice fringes are clearly seen without any apparent defects or grain boundaries. The distance between lattice fringes was of 0.29 and 0.32 nm, corresponding respectively to the inter-planar spacing of (001) and (110) planes

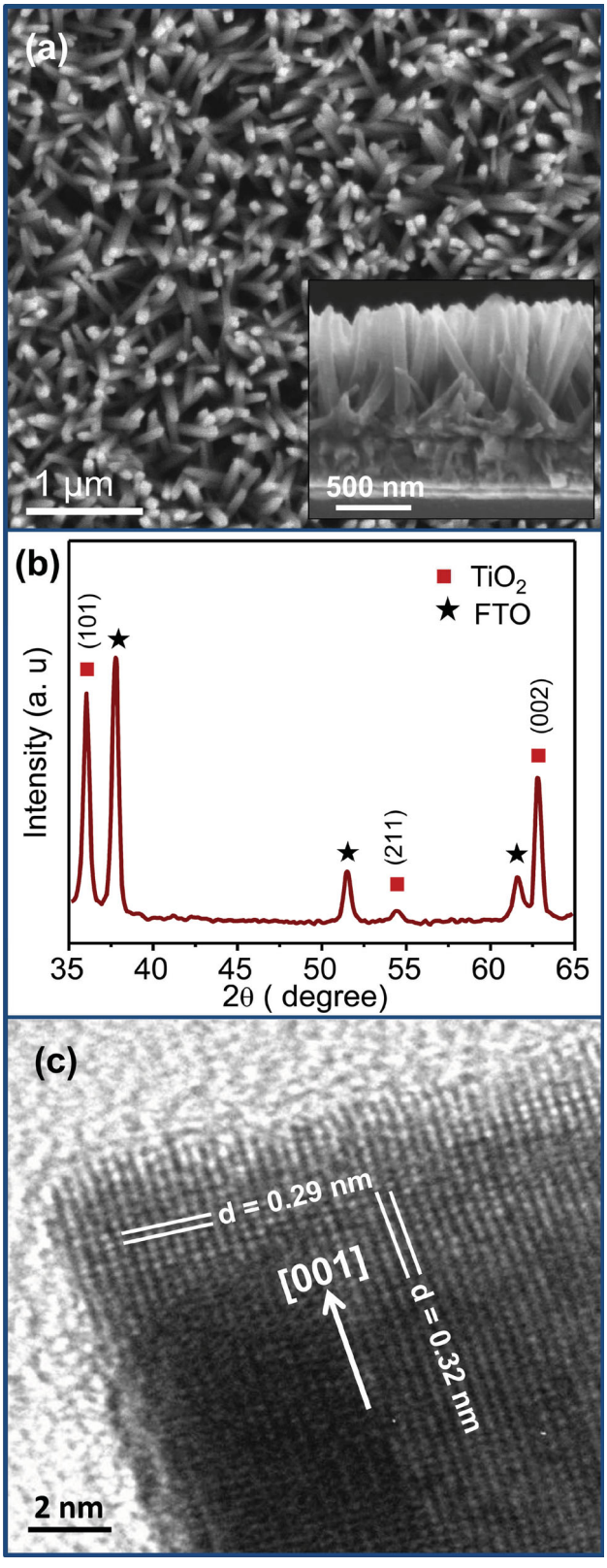

Figure 1. a) Typical top-view SEM image of the TiO_2-NRs. The inset shows a cross-section view of the vertically aligned NRs. b) XRD spectrum of the TiO_2-NRs grown onto FTO substrates precoated with ≈40 nm seed layer. c) High-resolution TEM image of a monocrystalline TiO_2-NR.

of the rutile phase. This suggests (001)-preferential growth of the NRs which is likely perpendicular to the substrate.[19] The presence of the TiO_2 seed layer is believed to promote the vertical growth of the NRs, as it facilitates the rapid formation of homo-nucleation sites and ensures a good adhesion to the substrate of the growing NRs. By improving the integrity and stability of the NRs-FTO interface, through the presence of this adhesion-seed-layer, the loss of photocharges is also expected to be significantly reduced.[17]

In order to form the NH-HJs, the PbS-QDs were PLD-deposited at room temperature, directly onto TiO_2-NRs coated FTO substrates. By varying the number of the KrF laser ablation pulses (N_{Lp}), from 2000 to 20 000, we have controlled the surface density of the QDs onto the surface of TiO_2-NRs and ultimately the thickness of the PbS-QDs films. The average diameter of the PbS-QDs does not vary much beyond $N_{Lp} \geq 1000$ pulses.[14] It tends to stabilize around ≈9 nm for higher N_{Lp} values. The PbS-QDs were PLD-deposited onto TiO_2-NRs having different lengths in order to identify the optimal NR length that provides the maximal interfacial area between TiO_2-NRs and PbS-QDs. **Figure 2**a,b show typical top-view SEM images of the TiO_2-NRs after their PLD coating with PbS-QDs at increasing N_{Lp} (namely, 2000 and 10 000, respectively). They clearly show the TiO_2-NRs uniformly coated with PbS-QDs with a cauliflower-like pebbly morphology of their domed tops (in contrast to their clean and flat squared-surface before PbS-QDs deposition, shown in Figure 1a). It is also worth noting that as N_{Lp} is increased from 2000 to 10 000, the PbS-QDs layer thickens and porosity gaps between the NRs are progressively filled up with the top of the NRs almost coalescing at high N_{Lp} values (Figure 2b). The cross-sectional SEM observation at a higher magnification of the TiO_2-NRs decorated with 2000 pulses of PbS-QDs (Figure 2c) reveals an "asparagus tip"-like morphology where nodules (i.e., PbS-QDs) are seen to conformally coat the NRs all along from their top down to their base with a surface coverage that seems to decrease as we are getting deeper between the NRs. Figure 2c is an important one as it provides evidence of the capacity of the PLD process to achieve relatively easily nanohybrid structures where vertically aligned TiO_2-NRs complex nanoarchitectures are conformally coated with PbS-QDs. This figure shows that the PbS-QDs cover the surface of TiO_2-NRs down to a certain depth from the surface, which is highly likely determined by the rate at which the lateral dimension of the NR tip thickens until the gap is closed between neighboring NRs. Thus, one would anticipate that there should be an optimal length for the TiO_2-NRs, that is close to the effective penetration depth of PLD PbS-QDs into TiO_2-NRs, as will be discussed later. Finally, Figure 2d shows the XRD patterns of the PbS-QDs films (N_{Lp} = 20 000) PLD-deposited on the porous TiO_2-NRs. It confirms the crystalline

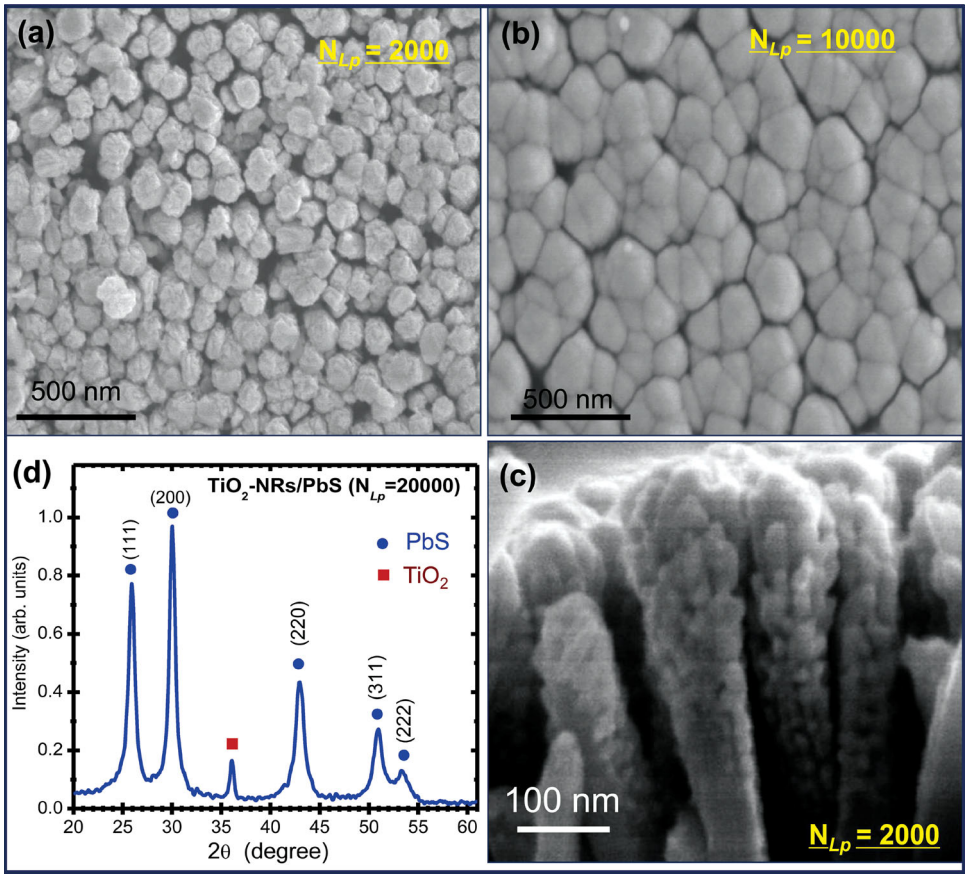

Figure 2. Top-view SEM images of the TiO_2-NRs PLD-coated with PbS-QDs with a) N_{Lp} = 2000 and b) N_{Lp} = 10 000; c) High-magnification cross-sectional SEM image of the TiO_2-NRs after their decoration with PbS-QDs at N_{Lp} = 2000; d) Typical X-ray diffraction spectrum of the PLD-deposited PbS-QDs (at N_{Lp} = 20 000) ontoTiO$_2$-NRs coated FTO substrates.

cubic phase of the PbS-QDs' film with relatively broad diffraction peaks, which can be attributed to the nanosize of PbS crystallites. Indeed, by using the Scherrer formula,[20] we have estimated the average crystallite size of the PbS QDs to be of about (9.3 ± 0.9) nm, which is consistent with the average size of the smallest features on the TiO_2-NRs of Figure 2c. Thus, by varying the N_{Lp}, we can control the total amount of deposited PbS-QDs (i.e., the equivalent thickness of the QDs film). From cross-section SEM observations of PbS-QDs film deposited onto flat-Si at N_{Lp} = 10 000, we have estimated its thickness to ≈390 nm. This yields a PbS-QDs nominal deposition rate of ≈0.04 nm per laser ablation pulse. This deposition rate of PbS-QDs is however expected to be locally lower onto the TiO_2-NRs' surface because of their porous structure and associated large surface area (in comparison to mirror-polished flat Si substrates).

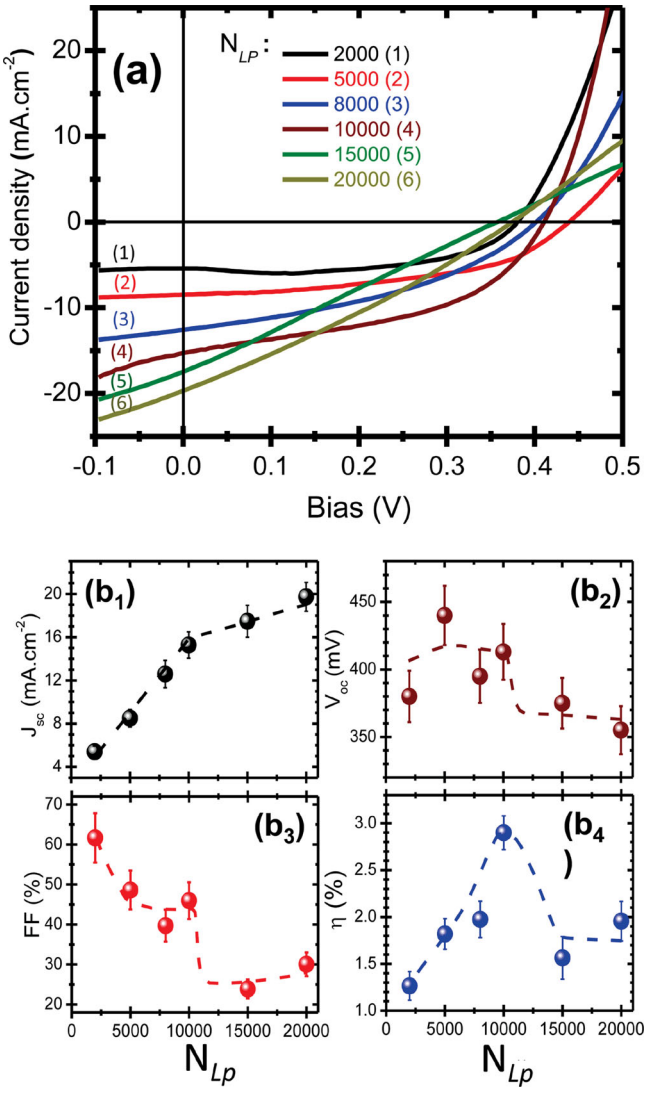

Figure 3. a) Typical *J–V* characteristics, measured under AM1.5 solar simulator, of the NH-HJs devices made with different amounts (N_{Lp}) of PbS-QDs; b1–b4):N_{Lp} dependence of the characteristics (J_{sc}, V_{oc}, FF, and η, respectively) of the NH-HJs PV devices. The error bars represent measurement fluctuations from different devices. (The dashed lines are added to guide the eye.)

To build the PV devices, the FTO-glass was used as a substrate onto which a ≈1.2 µm-thick film of vertically aligned TiO_2-NRs was hydrothermally grown. The PLD was used to decorate the TiO_2-NRs with PbS-QDs, and then Au electrodes (100 nm-thick) were evaporated on the TiO_2-NRs/PbS-QDs structure. These FTO/TiO_2-NRs/PbS-QDs structures were first optimized with respect to the amount of PbS-QDs to be deposited, by varying N_{Lp} from 2000 to 20 000. By systematically examining the cross-section SEM images of the TiO_2-NRs before and after PLD deposition of the PbS-QDs, we found that, regardless of the value of N_{Lp}, the penetration depth of the QDs into the NRs arrays was estimated to ≈300 nm, as can be seen in Figure 2c. The fact that the penetration depth for the PLD deposited PbS-QDs is insensitive to N_{Lp}, for a given TiO_2 NRs' length, is rather predictable as the QDs will continue to "infiltrate" the NRs array as long as the gaps between the NRs are still open and its top surface not completely clogged. This "clogging" is mainly controlled by the lateral thickening of the top of the TiO_2 nanorods following their coating with PbS-QDs.

Figure 3a shows the current density–voltage (*J–V*) characteristics of our NH-HJs based PV devices made with ≈1.2 µm-long TiO_2-NRs and different N_{Lp} values of PbS-QDs, under AM1.5 solar irradiation. The N_{Lp} dependence of the various PV parameters of the NH-HJs devices is summarized in Figure 3b_1–b_4. First of all, the short-circuit current density (J_{sc}) is seen (Figure 3b_1) to increase continuously up to N_{Lp} = 10 000 and then tend to saturate. This indicates that, up to N_{Lp} = 10 000, increasing the amount of PLD-deposited PbS-QDs leads to an increased light absorption of the devices and its efficient conversion into higher collected photocurrents. For higher N_{Lp} values (> 10 000), J_{sc} continues to increase but at much lower pace (doubling N_{Lp} from 10 000 to 20 000 has led to only 18% increase of J_{sc} versus an increase of 320% when N_{Lp} was increased from 2000 up to 10 000). This much slower increase of J_{sc} and its tendency to saturate pinpoint the existence of an optimum value of N_{Lp} (around 10 000) beyond which the photogeneration process is somehow less efficient. This N_{Lp} dependence of J_{sc} is thought to be due to a progressive increase of the series resistance of the devices as N_{Lp} is increased for N_{Lp} ≥ 10 000, which is caused by the increasing thickness of the surplus layer of PbS-QDs lying on the top of the nanorods. On the other hand, the open circuit voltage (V_{oc}) (Figure 3b_2) is found to remain roughly constant around a value of ≈0.42 V for N_{Lp} values ≤ 10 000 and then slightly decreases to a value around 0.37 V for N_{Lp} > 10 000. The FF is also seen to undergo a decrease from ≈45% to ≈24% when N_{Lp} exceeds 10 000 (Figure 3b_3). In order to assess the overall performance of our NH-HJs devices, Figure 3b_4 shows the N_{Lp} dependence of their PCE (η), where the highest η value of 2.9% is obtained for the optimal N_{Lp} = 10 000.

To further improve the PCE of our NH-HJs devices, we firstly fixed the N_{Lp} at the above-identified optimal value of 10 000; secondly, we inserted a 10 nm-thick MoO_3 hole extraction layer between the PbS-QDs top-layer and the Au electrodes; and finally, we varied the length of the TiO_2-NRs in the 120–2400 nm range. The devices were labeled with the length of their corresponding TiO_2-NRs (for instance, devices made

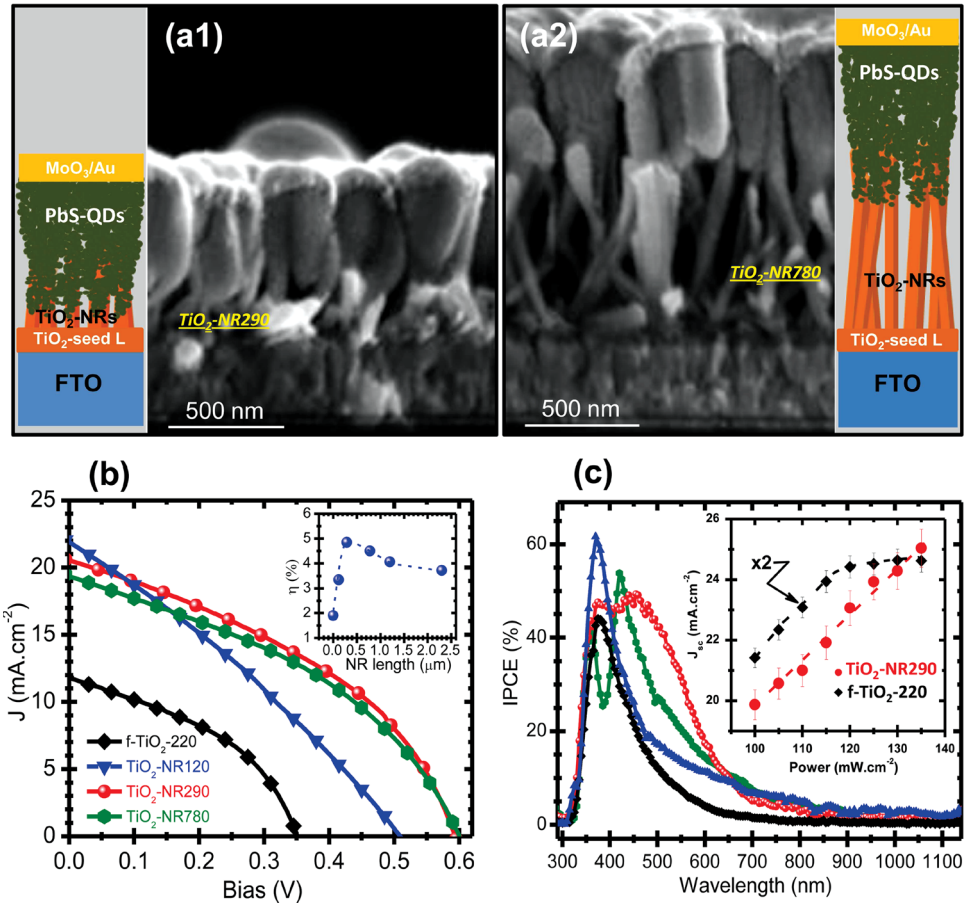

Figure 4. a1,a2) Cross-section SEM images of the NH-HJs devices made respectively with TiO_2-NRs' lengths of 290 and 780 nm, L = layer; b) Typical *J–V* curve, obtained under AM1.5 illumination, of the different NH-HJs devices as a function of the NR length while comparing them to that of flat sputter-deposited TiO_2 film (f-TiO_2_220); The inset in (b) shows the PCE variation as a function of the TiO_2-NR length; c) IPCE spectra of the NH-HJs devices fabricated with different lengths of TiO_2-NRs compared with that of f-TiO_2_220 device; The inset in (c) shows the J_{sc} variation as a function of the illuminating power of both TiO_2-NR290 and f-TiO_2_220 devices.

with 290 nm-long TiO_2-NRs were labeled as TiO_2-NR290). For comparison purposes, we have also fabricated devices with a sputter-deposited continuous flat TiO_2 films having a thickness 220 ± 5 nm (labeled as f-TiO_2_220). **Figure 4**a_1,a_2 present respectively the cross-sectional SEM image of freshly cleaved TiO_2-NR290 and TiO_2-NR780 devices, together with their associated schematic representations. The PbS-QDs are seen to coat the TiO_2-NRs while "infiltrating" their porous structure up to a certain penetration depth and to form a surplus top-layer of PbS-QDs (i.e., a sort of "canopy" on the top of the TiO_2 nanorods). The penetration depth of the PbS-QDs was estimated from the cross-sectional SEM images to be in the (250–350) nm range depending on the TiO_2-NR lengths and associated porosity. The *J–V* curves of the various PV devices with different TiO_2-NRs lengths together with that of the f-TiO_2_220 reference PV device, all obtained under a 1.5AM solar illumination, are shown in Figure 4b. First of all, the nanostructuration of the TiO_2 layer (i.e., NRs instead of flat TiO_2 film) and the presence of the MoO_3 layer are seen to impact significantly the collected J_{sc} (from ≈12 to ≈20 mA cm^{-2}), but also to increase the V_{oc} value from 0.35 V (for the f-TiO_2_220 devices) to 0.6 V (for the TiO_2-NR780 devices). This V_{oc} increase is due to the insertion of the MoO_3 layer.[7,21,22] The MoO_3 HEL has been shown to be very effective in improving the charge transfer between the PbS-QDs and metal electrodes. The recent work of Brown et al.[7] have clearly shown that the addition of a MoO_3 HEL layer, in the case of heterojunction PV devices based on ZnO and chemically-processed PbS-QDs, significantly improves the overall PCE of the devices. This improved charge transfer is a consequence of the high work function of MoO_3 which is found to pin the Fermi level of the Au electrode, enabling thereby the formation of an Ohmic contact to PbS-QDs and allowing even low-work function metals to be used as anodes without forming a voltage-limiting Schottky contact.[22] It has also been reported that the hole transport from PbS-QDs to the metal electrode through the MoO_x HEL is facilitated by the existence of bandgap states caused by the oxygen vacancies of the MoO_x layer, as evidenced by the UV-photoemission spectroscopy (UPS) measurements, through the study of the interfacial energy levels between MoO_x and PbS-QD layer.[22] Thus, Gao et al. have shown that the intercalation of a MoO_x HEL between PbS-QDs and various metal electrodes (Al, Ag, Au) has led to an important increase in the PCE of their chemically-processed (ZnO nanocrystals/PbS-QDs) heterojunction based PV devices.[22] They concluded that

a possible acting mechanism of the HEL is a dipole formed at the MoO_3 and PbS interface enhancing band bending to allow efficient hole extraction from the valence band of the PbS-QDs.

Secondly, by comparing the various NR lengths, Figure 4b reveals that the TiO_2-NR290 devices exhibit both the highest V_{oc} value of 600 mV with a J_{sc} of 20.54 mA cm^{-2}, leading thereby to the achievement of a PCE value as high as 4.85% for the TiO_2-NR290 devices (≈155% more efficient than the η of 1.9% exhibited by their f-TiO_2_220 devices counterpart). Decreasing the TiO_2-NRs' length to 120 nm (i.e., TiO_2-NR120 devices) was found to yield a maximum PCE of 3.34 ± 0.2%, which is lower than that of TiO_2-NR290 devices, while still being higher than the PCE of the f-TiO_2_220 devices. On the other hand, increasing the length of TiO_2-NRs to 780 nm (i.e., TiO_2-NR780 devices) does not improve the PCE (which is found to decrease to 4.5 ± 0.2%). Further increasing the NR length up to 2.4 µm was found to yield lower PCE values of ≈3.8%. The η dependence on the TiO_2-NRs' length is summarized in the inset of Figure 4b. These results clearly highlight the effect of the length of the TiO_2-NRs in the photogeneration and collection processes, and point out the existence of an optimal NR length (around 290 nm) that leads to the highest PCE of 4.85%. This high η value is believed to be due to the fact that the length of the TiO_2 nanorods (≈290 nm) is quite close to the penetration depth (300 ± 50 nm) of PbS-QDs into the TiO_2-NR matrix. This leads to the formation of the largest extent of NH heterojunctions through the device structure while shortening photocharges pathways towards collecting electrodes. More importantly, the PCE of our NH-HJs devices was found to remain very stable over time. Indeed, **Figure 5** shows that, regardless of the TiO_2-NR's length, the relative variation of the PCE of our devices follows the same trend; that is a slight relative decrease of ≈15% after 6 months and ≈27% after 14 months of their on-shelf storage in ambient air with no specific encapsulation. This highlights the excellent stability of the laser synthesized PbS-QDs based PV devices when compared to that of similar devices using chemically-synthesized PbS-QDs, of which PCE generally undergoes drastic and rapid relative decrease (from ≈20% to more than 70% in the few days following their fabrication if no encapsulation is used and/or caution is taken to prevent the rapid oxidation of the PbS-QDs.[23–25]

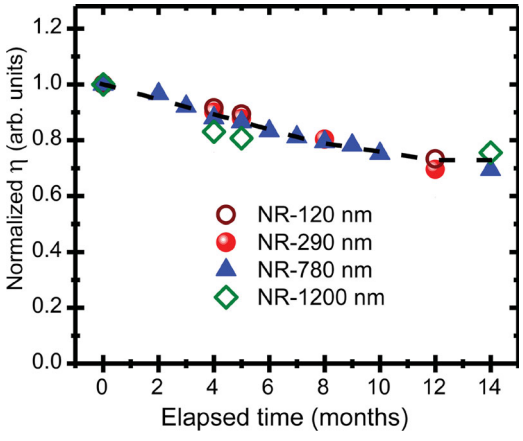

Figure 5. Time stability, under ambient air, of the normalized PCE of the various NH-HJs based PV devices for the different TiO_2-NR lengths (i.e., 120, 290, 780, and 1200 nm).

To gain more insights in the photogeneration process of our NH-HJs PV devices, the incident photon-to-current efficiency (IPCE) spectra were systematically measured for the various devices. Figure 4c compares the IPCE spectra of the TiO_2-NR290, TiO_2-NR120, TiO_2-NR780, and f-TiO_2_220 devices. It is clearly seen that the photogeneration of our PV devices spans the entire 380–900 nm wavelength range with a more pronounced photoconversion in the 380–600 nm range (with IPCE values in the 15–65% range, depending on the device characteristics). The f-TiO_2_220 and TiO_2-NR120 devices are found to exhibit a relatively narrow IPCE spectra centered around 380 nm (corresponding to the bandgap of TiO_2), with a more pronounced IPCE maximum for the TiO_2-NR120 in comparison with f-TiO_2_220 devices (≈60% versus ≈40%, respectively). In contrast, the IPCE spectra of both TiO_2-NR290 and TiO_2-NR780 devices are seen to broaden and present two overlapping peaks. Interestingly, the broadest IPCE spectrum of the TiO_2-NR290 devices correlates well with their highest PCE of η = 4.85%, revealing thereby their capacity to harvest photons in a much wider light range (with an IPCE in the 30–50% range over all the 350–550 nm range). The double-peak structure of the broad IPCE of the TiO_2-NR290 and TiO_2-NR780 devices is thought to result from the convolution of two opposite tendencies, namely the decreasing absorbance of TiO_2-NRs (for λ > 380 nm) and the rising absorbance of PbS-QDs (which significantly rises for shorter wavelengths). The magnitude and thereby the spectral position of the IPCE component associated with PbS-QDs depends on the effective amount of PbS being exposed to light and contributing to the photogeneration process of the devices (keeping in mind that the PV devices are illuminated from the FTO side). Figure 4c also provides a clear-cut evidence of the contribution of PbS-QDs into the PV process, as IPCE values in the 10–50% range are obtained all over the 400–700 nm spectral range, well below the bandgap of TiO_2. On the other hand, the inset of Figure 4c shows that the J_{sc} of TiO_2-NR290-devices linearly increases with the intensity of the sun light, while it tends to saturate for f-TiO_2_220 devices for light irradiances higher than 115 mW cm^{-2}. This shows the capacity of these nanostructured NH-HJs based devices to harvest more photons and to collect more efficiently the created photocharges.

Finally, based on our recent results on the laser ablation synthesized single wall carbon nanotubes/PbS-QDs (SWCNTs/PbS-QDs) nanohybrids),[11] we have replaced the PbS-QDs in the above-presented PV devices by SWCNTs/PbS-QDs nanohybrids, and investigated their PV properties. Indeed, the SWCNTs/PbS-QDs nanohybrids have been shown to exhibit not only efficient and fast charge transfer from the QDs to SWCNTs but also an optical absorption higher than that of the bare PbS-QDs. Briefly, the SWCNTs/PbS-QDs based solar cells were made by first spray coating SWCNTs on the TiO_2-NRs (with the optimal length of ≈290 nm), and then a direct laser ablation deposition of PbS-QDs was used to decorate the SWCNTs. (The details of the synthesis of SWCNTs and their spray-deposition for achieving PV devices can be found elsewhere).[26,27] **Figure 6**a,b show typical top-view SEM images of the TiO_2-NRs covered by SWCNTs before and after the PLD deposition of the PbS-QDs, respectively. SWCNTs bundles are seen to surround the TiO_2-

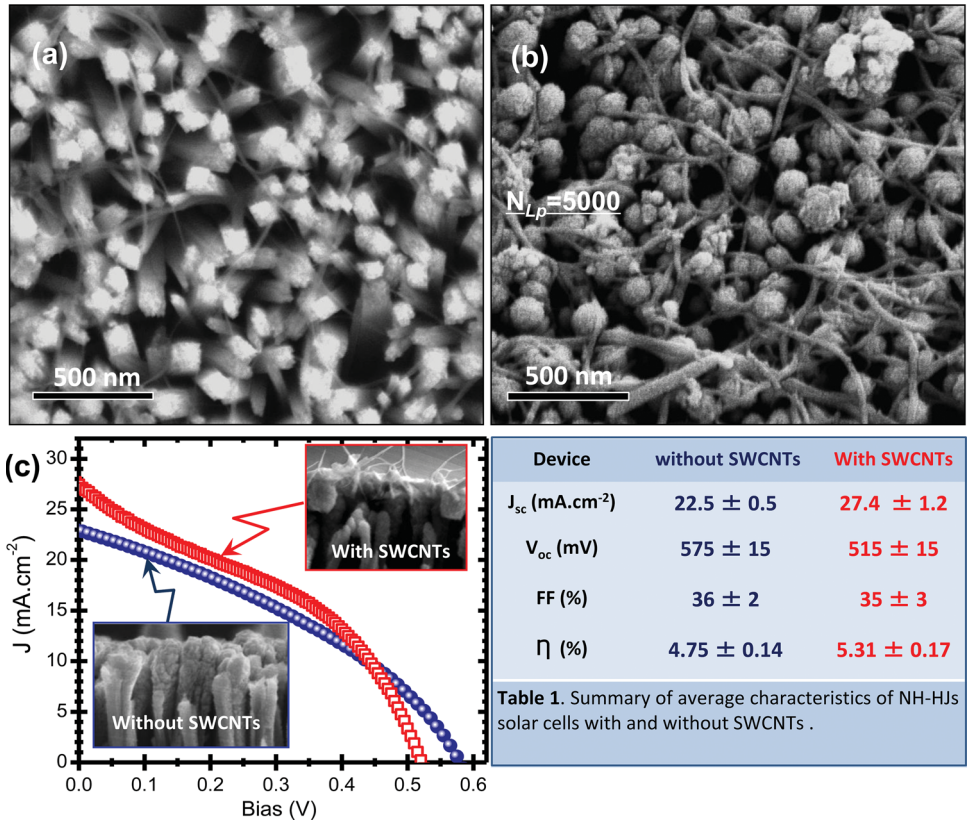

Device	without SWCNTs	With SWCNTs
J_{sc} (mA.cm^{-2})	22.5 ± 0.5	27.4 ± 1.2
V_{oc} (mV)	575 ± 15	515 ± 15
FF (%)	36 ± 2	35 ± 3
Η (%)	4.75 ± 0.14	5.31 ± 0.17

Table 1. Summary of average characteristics of NH-HJs solar cells with and without SWCNTs .

Figure 6. Typical top-view SEM images of TiO_2-NRs after their spray-coating by SWCNTs a) before and b) after their subsequent PLD-decoration by PbS-QDs; c) Typical *J–V* curves of the NH-HJs devices with and without the addition of SWCNTs and PbS-QDs (at the optimal N_{LP} of 10 000 and TiO_2-NRs' length of 290 nm).

NRs and penetrate between them (Figure 6a). The PLD of PbS-QDs provides a conformal coating of both the SWCNTs and the TiO_2-NRs, as shown in Figure 6b. By integrating these novel PbS-QDs/SWCNTs/TiO_2-NRs nanohybrids into PV devices, we were able to assess their PV performance. Figure 6c compares the *J–V* curves of these NH-HJs based devices with and without the addition of SWCNTs. The addition of SWCNTs is found to enhance significantly the J_{sc} while slightly lowering the V_{oc}. Table 1 in Figure 6 presents a comparative summary of the PV characteristics of the NH-HJs devices with and without the addition of SWCNTs (these data represent the averaged values of 15 different devices made onto different substrates). On average, the addition of SWCNTs is found to lead to an increase of J_{sc} by ≈21% in comparison with the devices not containing SWCNTs. This SWCNTs induced J_{sc} increase can be explained by examining the band diagram of the NH-HJs devices. Indeed, while **Figure 7**a shows the energy levels for the various materials used in the fabrication of the PV devices, Figure 7b,c compare the band alignments of both TiO_2-NRs/PbS-QDS and TiO_2-NRs/SWCNTs/PbS-QDS structures, respectively. It is clearly seen that the p-n junctions formed between TiO_2-NRs and PbS-QDs (Figure 7b) lead to the creation of a depletion field that favors the extraction of the photogenerated charges, where electrons are injected in the TiO_2 and collected by the FTO electrode and holes travel to the Au electrode through the MoO_3 HEL interlayer. This TiO_2/PbS junction can nonetheless be further improved through the addition of a SWCNTs layer, as SWCNTs are indeed often used to extract electrons from QDs.[28,29] This favorable charge pathway can be easily deduced from the band diagram alignment depicted in Figure 7b. Indeed, the conduction band of SWCNTs is seen to be located between the conduction bands of PbS and TiO_2, facilitating thereby the electron injection into TiO_2 which, in turn, is expected to enhance the collected current of the TiO_2-NRs/SWCNTs/PbS-QDs, in accordance with the results of Figure 6c. In other words, the incorporation of SWCNTs provides favorable and "smoother" energetic transition (i.e., reduced band bending at the TiO_2 interface) for the electrons to be injected into TiO_2. On the other hand, possible contribution of SWCNTs to the generation of photocurrent in the devices cannot be excluded, as this has been recently invoked in the case of p-n junctions consisting of p-type double-wall-CNTs and n-type TiO_2 nanotube arrays.[30] Moreover, SWCNTs form an effective backbone of 1D nanowires that enhance the charge transport among semiconducting QDs (where otherwise the inter-particle random hopping can limit the efficiency of charge transfer).[31] Thus, the enhanced J_{sc} exhibited by the PbS-QDs/SWCNTs/TiO_2-NRs based PV devices is thought to be a consequence of the synergistic charge separation and efficient transport provided by the presence of SWCNTs. This J_{sc} enhancement however comes at a cost of a slight V_{oc} decrease (from ≈575 mV for the devices without SWCNTs to ≈515 mV for those with SWCNTs), which is attributed to the slightly lower work function of SWCNTs in comparison with that of PbS (i.e., ≈4.7 eV for SWCNTs[32] versus

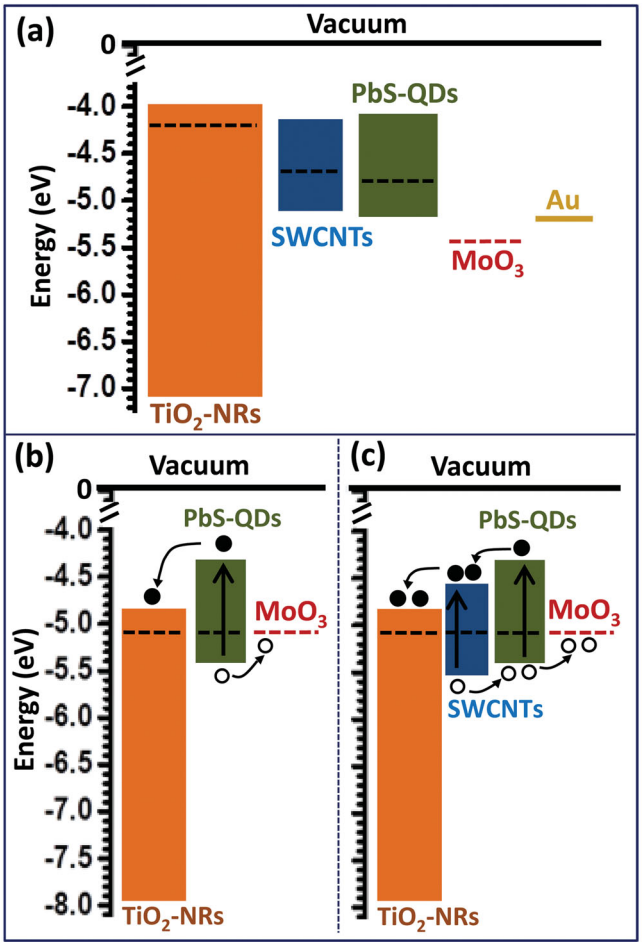

Figure 7. a) Schematic representation of the energy-level diagram of the different materials used for the fabrication of our NH-HJ PV devices. Comparison of the excitation and charge transfer pathways for both the b) TiO_2-NRs/PbS-QDs and c) TiO_2-NRs/SWCNTs/PbS-QDs nanohybrid heterojunctions.

≈4.8 eV for PbS-QDs).[33] In sum, the NH-HJs devices with SWCNTs were found to exhibit an average PCE value as high as 5.3%, demonstrating clearly the beneficial effect of adding SWCNTs into the devices. This significant improvement of the PCE by 11.7% is mainly due to the most important increase of J_{sc}. These promising results suggest that further optimization of the deposited amount and electro-optical properties of the SWCNTs layer could result into higher PV performance, as recently demonstrated for SWCNTs based PV devices.[26,27]

3. Conclusion

In summary, we have demonstrated the potential of PLD as a powerful and straightforward method to decorate controllably and conformally one-dimensional nanostructures (e.g., TiO_2-NRs and SWCNTs) with PbS-QDs, leading thereby to the achievement of novel nanohybrid heterojunctions without resorting to any surface treatment, ligand engineering and/or post-synthesis processing. Thus, we were able to develop TiO_2-NRs/PbS-QDs PV devices and optimize their PV performance through a systematic study of both the amount of deposited PbS-QDs (i.e., N_{Lp}) and the length of the TiO_2-NRs. This work has led to the achievement of optimal NH-HJs based devices with a high PCE of 4.85%, which was found to be fairly stable for several months under ambient air. The addition of SWCNTs into these NH-HJ structures to improve their photocharge collection has been shown to further enhance their PCE to a value as high as 5.3%. These promising results pave the way for more systematic investigations for the optimization and better understanding of the role of SWCNTs in the photogeneration process in these complex NH structures.

4. Experimental Section

TiO_2-Nanorods Synthesis: Prior the growth of the TiO_2-NRs, a thin TiO_2 seed layer (~40 nm-thick) was deposited onto the FTO substrates by an RF-magnetron sputtering (13.56 MHz) process at a substrate temperature of 550 °C (more details about the sputter-deposition of TiO_2 can be found elsewhere).[34] The FTO glass substrates (1" × 1" size) were previously cleaned using ultrasonic bath consecutively with isopropanol, ethanol and pure water for 15 min each, and then air dried. The cleaned substrates were introduced into the hydrothermal vessel to grow the TiO_2-NRs based on literature.[19] The length of the TiO_2-NRs was controlled through reaction time. After the hydrothermal growth, the substrates covered with TiO_2-NRs were rinsed thoroughly with dilute HCl acid, then with pure water and dried in air.

Synthesis of the PbS-QDs Film: Prior to the PLD deposition of PbS-QDs, the vacuum chamber was turbo-pumped down to 10^{-6} mTorr, and then deposition was performed under a helium background pressure of 500 mTorr. The KrF ablation laser (λ = 248 nm; pulse duration = 14 ns; repetition rate = 20 Hz) was focused onto a rotating PbS pellet placed at a distance of 7.5 cm from the substrate. The on-target laser intensity was set to 2.5 10^8 W cm^{-2}, and the PLD was performed at room temperature (RT). More detailed description of the PLD synthesis of PbS QDs can be found elsewhere.[14]

I–V and IPCE Characterization: The *I–V* characteristics of the NH-HJs based PV devices were systematically measured in ambient atmosphere under dark and AM1.5 calibrated solar simulator. The data acquisition was performed by using an Agilent B2901A unit. The active area of the devices is circular with diameter of 1 mm. The spectrally resolved IPCE of the NH-HJs devices was measured at RT in ambient atmosphere using a xenon arc lamp passing through a monochromator. The monochromatic light is then chopped at a frequency of 6 Hz and focused onto the sample. The active area was the same as for *I–V* measurements. The photocurrent at each wavelength $I(\lambda)$ is measured with a lock-in amplifier (Ametek 1256) at zero bias. The light power at each wavelength $P(\lambda)$ is measured, through the same circular aperture of 1 mm diameter, with a calibrated photodiode (Newport 918D) placed at the same position of the device. Then, the IPCE value at each wavelength is determined as follows: $100\ h\ c\ I(\lambda)/q\ \lambda\ P(\lambda)$, where c is the speed of light, h is the Planck constant, and q is the electronic charge. More details on the IPCE measurements can be found elsewhere.[35]

Acknowledgments

The authors would like to acknowledge the financial support from the Natural Sciences and Engineering Research Council (NSERC) of Canada through Discovery and Strategic grants, the FRQNT (Le Fonds de Recherche du Québec-Nature et Technologies) through its strategic Network "Plasma-Québec", and Nano-Québec (the Québec Organization for the promotion of nanoscience and nanotechnologies).

Received: December 17, 2013
Revised: January 29, 2014
Published online: March 19, 2014

[1] L. Etgar, D. Yanover, R. K. Capek, R. Vaxenburg, Z. Xue, B. Liu, M. K. Nazeeruddin, E. Lifshitz, M. Grätzel, *Adv. Funct. Mater.* **2013**, *23*, 2736.
[2] J. Gao, J. M. Luther, O. E. Semonin, R. J. Ellingson, A. J. Nozik, M. C. Beard, *Nano Lett.* **2011**, *11*, 1002.
[3] K. W. Kemp, A. J. Labelle, S. M. Thon, A. H. Ip, I. J. Kramer, S. Hoogland, E. H. Sargent, *Adv. Energy Mater.* **2013**, *3*, 917.
[4] J. Seo, S. J. Kim, W. J. Kim, R. Singh, M. Samoc, A. N. Cartwright, P. N. Prasad, *Nanotechnology* **2009**, *20*, 095202.
[5] C. Kuo, M. Su, C. Ku, S. Wang, H. Leeb, K. Wei, *J. Mater. Chem.* **2011**, *21*, 11605.
[6] A. G. Midgett, J. M. Luther, J. T. Stewart, D. K. Smith, L. A. Padilha, V. I. Klimov, A. J. Nozik, M. C. Beard, *Nano Lett.* **2013**, *13*, 3078.
[7] P. R. Brown, R. R. Lunt, N. Zhao, T. P. Osedach, D. D. Wanger, L. Chang, M. G. Bawendi, V. Bulovi, *Nano Lett.* **2011**, *11*, 2955.
[8] O. E. Semonin, J. M. Luther, S. Choi, H.-Y. Chen, J. Gao, A. J. Nozik, M. C. Beard, *Science* **2011**, *334*, 1530.
[9] J. Tang, K. Kemp, S. Hoogland, K. S. Jeong, H. Liu, L. Levina, M. Furukawa, X. Wang, R. Debnath, D. Cha, K. W. Chou, A. Fischer, A. Amassian, J. B. Asbury, E. H. Sargent, *Nat. Mater.* **2011**, *10*, 765.
[10] X. Lan, J. Bai, S. Masala, S. M. Thon, Y. Ren, I. J. Kramer, S. Hoogland, A. Simchi, G. I. Koleilat, D. Paz-Soldan, Z. Ning, A. J. Labelle, J. Y. Kim, G. Jabbour, E. H. Sargent, *Adv. Mater.* **2013**, *25*, 1769.
[11] I. Ka, V. Le Borgne, D. Ma, M. A. El Khakani, *Adv. Mater.* **2012**, *24*, 6289.
[12] B. Li, J. Liu, G. Xu, R. Lu, L. Feng, J. Wu, *Appl. Phys. Lett.* **2012**, *101*, 153903.
[13] Q. Dai, J. Chen, L. Lu, J. Tang, W. Wang, *Nano Lett.* **2012**, *12*, 4187.
[14] I. Ka, D. Ma, M. A. El khakani, *J. Nanopart. Res.* **2011**, *13*, 2269.
[15] H. W. Kim, D. S. Kwak, Y. J. Kwon, C. Lee, J. H. Jung, *Met. Mater. Int.* **2013**, *19*, 1123.
[16] M. Gaidi, A. Hajjaji, R. Smirani, B. Bessais, M. A. El Khakani, *J. Appl. Phys.* **2010**, *108*, 063537.
[17] W. Yang, F. Wan, S. Chen, C. Jiang, *Nanoscale. Res. Lett.* **2009**, *4*, 1486.
[18] T. S. Senthil, A.-Y. Kim, N. Muthukumarasamy, M. Kang, *J. Sol-Gel Sci. Technol.* **2013**, *67*, 420.
[19] X. Feng, K. Shankar, O. K. Varghese, M. Paulose, T. J. Latempa, C.A. Grimes, *Nano Lett.* **2008**, *8*, 3781.
[20] J. Gao, S. Jeong, F. Lin, P. T. Erslev, O. E. Semonin, J. M. Luther, M. C. Beard, *Appl. Phys. Lett.* **2013**, *102*, 043506.
[21] X. Wang, G. I. Koleilat, A. Fischer, J. Tang, R. Debnath, L. Levina, E. H. Sargent, *ACS. Appl. Mater. Interfaces* **2011**, *3*, 3792.
[22] J. Gao, C. L. Perkins, J. M. Luther, M. C. Hanna, H.-Y. Chen, O. E. Semonin, A. J. Nozik, R. J. Ellingson, M. C. Beard, *Nano Lett.* **2011**, *11*, 3263.
[23] G. Zhai, A. Bezryadina, A. J. Breeze, D. Zhang, G. B. Alers, S. A. Carter, *Appl. Phys. Lett.* **2011**, *99*, 063512.
[24] J. Tang, X. Wang, L. Brzozowski, D. A. R. Barkhouse, R. Debnath, L. Levina, E. H. Sargent, *Adv. Mater.* **2010**, *22*, 1398.
[25] S. H. Im, H.-J. Kim, S. Kim, S.-W. Kim, S. Seok, *Org. Electron.* **2012**, *13*, 2352.
[26] V. Le Borgne, B. Aissa, M. Mohamedi, Y. A. Kim, M. Endo, M. A. El Khakani, *J. Nanopart. Res.* **2011**, *13*, 5759.
[27] V. Le Borgne, L. A. Gautier, M. A. El Khakani, *Appl. Phys. Lett.* **2013**, *103*, 073103.
[28] B. J. Landi, S. L. Castro, H. J. Ruf, C. M. Evans, S. G. Bailey, R. P. Raffaelle, *Sol. En. Mat. Sol. Cells.* **2005**, *87*, 733.
[29] C. X. Guo, H. B. Yang, Z. M. Sheng, Z. S. Lu, Q. L. Song, C. M. Li, *Angew. Chem. Int. Ed.* **2010**, *49*, 3014.
[30] G. Zhang, J.-L. Sun, J. Wei, H. Sun, J.-L. Zhu, *Nanotechnology* **2013**, *24*, 465203.
[31] J. M. Lee, B.-H. Kwon, H. I. Park, H. Kim, M.G. Kim, J. S. Park, E. S. Kim, S. Yoo, D. Y. Jeon, S. O. Kim, *Adv. Mater.* **2013**, *25*, 2011.
[32] S. Shukla, T. Y. Ohulchanskyy, Y. Sahoo, M. Samoc, R. Thapa, A. N. Cartwright, P. N. Prasad, *J. Phys. Chem. C.* **2010**, *114*, 3180.
[33] I. J. Kramer, L. Levina, R. Debnath, D. Zhitomirsky, E. H. Sargent, *Nano Lett.* **2011**, *11*, 3701.
[34] D. Brassard, D. K. Sarkar, M. A. El Khakani, L. Ouellet, *J. Vac. Sci. Technol. A* **2006**, *24*, 600.
[35] V. Le Borgne, L. A. Gautier, P. Castrucci, S. Del Gobbo, M. De Crescenzi, M. A. El Khakani, *Nanotechnology* **2012**, *23*, 215206.